Effect of Austenite Stability on Microstructural Evolution and Tensile Properties in Intercritically Annealed Medium-Mn Lightweight Steels

HYEJIN SONG, SEOK SU SOHN, JAI-HYUN KWAK, BYEONG-JOO LEE, and SUNGHAK LEE

The microstructural evolution with varying intercritical-annealing temperatures of medium-Mn ($\alpha + \gamma$) duplex lightweight steels and its effects on tensile properties were investigated in relation to the stability of austenite. The size and volume fraction of austenite grains increased as the annealing temperature increased from 1123 K to 1173 K (850 °C to 900 °C), which corresponded with the thermodynamic calculation data. When the annealing temperature increased further to 1223 K (950 °C), the size and volume fraction were reduced by the formation of athermal α'-martensite during the cooling because the thermal stability of austenite deteriorated as a result of the decrease in C and Mn contents. In order to obtain the best combination of strength and ductility by a transformation-induced plasticity (TRIP) mechanism, an appropriate mechanical stability of austenite was needed and could be achieved when fine austenite grains (size: 1.4 μm, volume fraction: 0.26) were homogenously distributed in the ferrite matrix, as in the 1123 K (850 °C)—annealed steel. This best combination was attributed to the requirement of sufficient deformation for TRIP and the formation of many deformation bands at ferrite grains in both austenite and ferrite bands. Since this medium-Mn lightweight steel has excellent tensile properties as well as reduced alloying costs and weight savings, it holds promise for new automotive applications.

I. INTRODUCTION

REDUCTION in automotive vehicle weight has been emphasized in research and industrial areas of automotive steels so as to increase fuel efficiency and decrease greenhouse gases.[1,2] Automotive steels need excellent strength and ductility simultaneously, and thus, highly deformable high-strength steels have been actively developed by using deformation mechanisms such as transformation-induced plasticity (TRIP) and twinning-induced plasticity.[3–12] Besides, (ferrite + austenite) duplex lightweight steels, in which a considerable amount of Al is added to obtain the lightweight effect, have also been developed. It has been shown that the addition of 4 to 6 wt pct of Al results in 6 to 9 pct of weight saving in comparison to conventional automotive steels, and occasionally offers excellent properties such as strengths above 830 MPa and elongation above 40 pct.[3,13–15] Since the addition of Al generally reduces the ductility,[16–21] ($\alpha + \gamma$) duplex microstructures, where the austenite works as a secondary phase in ferrite matrix, have been favorably suggested.[3–6,13,14,22–27] From these microstructures, high-strength and high-ductility lightweight steels having high work-hardening capacity can be achieved by a deformation-induced austenite/martensite transformation, i.e., TRIP mechanism.[3–6]

In Fe-Mn-Al-C—based ($\alpha + \gamma$) duplex lightweight steels, Mn plays a role in promoting the formation of austenite because it acts as an austenite stabilizer.[28,29] This high addition of Mn, however, often causes problems such as reduced productivity due to the temperature drop of the molten steel during steelmaking, nozzle blocking during continuous casting, cracking during hot rolling, and surface oxidation of rolled steel sheets.[30] The reduction in Mn addition is not easy because the austenite-containing steel microstructure has to be stabilized at room temperature. Thus, many steel companies are actively developing medium-Mn ($\alpha + \gamma$) duplex lightweight steels containing about 10 wt pct of Mn and Al to achieve an excellent combination of strength and ductility as well as low alloying costs and lightweight effects.[3,13,14] According to research on Fe-5.8Mn-3.1Al-0.12C-0.47Si steel and Fe-3.5Mn-5.9Al-0.4C steel,[4,6] austenite grains retained at room temperature without κ-carbides were refined (size: 0.2 to 0.3 μm) and were transformed to α'-martensite during deformation to obtain the tensile strength

HYEJIN SONG, Research Assistant, and SEOK SU SOHN, Postdoctoral Research Associate, are with the Center for Advanced Aerospace Materials, Pohang University of Science and Technology, Pohang 790-784, Korea. Contact email: bbosil7@postech.ac.kr JAI-HYUN KWAK, Senior Principal Researcher, is with the Sheet Products & Process Research Group, Technical Research Laboratories, POSCO, Kwangyang 545-090, Korea. BYEONG-JOO LEE and SUNGHAK LEE, Professors, are with the Center for Advanced Aerospace Materials and also with the Department of Materials Science and Engineering, Pohang University of Science and Technology.

and ductility of 990 MPa and 28 pct, respectively. In order to achieve a more excellent combination of strength and ductility in the medium-Mn duplex light-weight steels, the effective use of a TRIP mechanism by properly controlling the mechanical stability of retained austenite is needed.[3–5,31–33] In addition, studies on how the size, volume fraction, and distribution of secondary phases such as austenite and martensite and resultant mechanical properties are affected by an intercritical-annealing treatment are also needed. Such a microstructural evolution occurring during various stages of deformation might play an important role in controlling the TRIP mechanism.

In this study, medium-Mn ($\alpha + \gamma$) duplex lightweight steels showing a TRIP mechanism were fabricated by varying the intercritical-annealing temperature, and the tensile properties were evaluated. In addition to the experimental approach, fractions of phases existing at high temperatures were verified by thermodynamic calculations. Detailed deformation mechanisms were investigated in relation to microstructural evolution by electron backscatter diffraction (EBSD) analyses, and they were correlated with the microstructural evolution process and with tensile strength and ductility. Appropriate microstructures of medium-Mn lightweight steels were suggested.

II. EXPERIMENTAL

A. Lightweight Steels

The lightweight steel examined in this study was fabricated by a vacuum induction melting method, and its chemical nominal composition was Fe-0.32C-5.8Mn-5Al-(<0.02)(P + S) (wt pct). Sixty-millimeter-thick plates homogenized at 1473 K (1200 °C) for 1 hour were hot rolled between 1373 K and 1173 K (1100 °C and 900 °C) to produce 3-mm-thick sheets, and were cooled in a furnace from 923 K (650 °C) after holding at this temperature for 1 hour to simulate a coiling procedure. A batch annealing treatment at 1023 K (750 °C) for 1 hour followed by furnace cooling was carried out in order to prevent edge cracks frequently formed during cold rolling.[34] The batch-annealed sheets were rolled to 1-mm thickness at room temperature. The cold-rolled sheets were intercritically annealed at 1123 K, 1173 K, and 1223 K (850 °C, 900 °C, and 950 °C) for 10 minutes at an Ar atmosphere and cooled in air. For convenience, the steel sheets annealed at 1123 K, 1173 K, and 1223 K (850 °C, 900 °C, and 950 °C) are referred to as 'A850,' 'A900,' and 'A950,' respectively. The density of the present lightweight steel was measured to be 7.2 g cm^{-3} by a densitometry (model: Mettler-Toledo XP205, Mettler-Toledo AG, Switzerland), based on Archimedes principle, which showed an apparent weight reduction of about 9 pct in comparison with pure Fe.

B. Microstructural Analysis

Phases present in the steels were identified by X-ray diffraction (XRD, Cu K_α radiation, scan rate:

2 deg min^{-1}, scan step size: 0.02 deg). The EBSD analysis (step size: 0.1 μm) was conducted by a field emission-scanning electron microscope (model: S-4300SE, Hitachi, Tokyo). The EBSD specimens were mechanically polished and then electropolished in a solution of 8 pct perchloric acid + 92 pct acetic acid at a voltage of 40 V. The data were interpreted by orientation imaging microscopy (OIM) analysis software (TSL OIM Analysis 5.2) provided by TexSEM Laboratories, Inc. Electron probe microanalysis (EPMA) measurements employing wavelength-dispersive spectrometry were also performed by an EPMA microprobe (model: JXA 8530F microprobe, JEOL, Tokyo) at an electron beam voltage of 15 keV. Since the precise measurement of C content in the EPMA was difficult, the C content was measured by the XRD method using the following equation:[35]

$$\alpha_\gamma = 3.578 + 0.0330X_C + 0.0056X_{Al} + 0.00095X_{Mn}$$
[1]

where α_γ is austenite lattice parameter (in Å) and X_C, X_{Mn}, and X_{Al} are concentrations of C, Mn, and Al, respectively (in wt pct). The austenite lattice parameter (α_γ) was determined from a d-spacing of (220)$_\gamma$ position. The volume fraction of austenite was measured by a direct comparison method using XRD analysis.[36] Integrated intensities of (200)α and (211)α peaks, (220)γ and (311)γ peaks were applied for this XRD method. It is known that the uncertainty of the fraction of austenite obtained from the XRD analysis is approximately 5 pct, although it can increase when the specimen has a preferred orientation.[37]

C. Tensile Test

Plate-type tensile specimens having gage length of 25 mm, gage width of 6 mm, and gage thickness of 1 mm were prepared in the longitudinal direction. They were tested at room temperature at a strain rate of 10^{-3} s^{-1} by a universal testing machine (model: 8801, Instron, Canton, MA) of 100-kN capacity. The tensile test was conducted three times for each datum point. In order to investigate crack initiation and propagation processes, the fracture surface and its cross-sectional area were observed by SEM.

III. RESULTS

A. Interpretation of High-Temperature Equilibrium Phases by Thermodynamic Calculation

Fractions of equilibrium phases and solute contents in ferrite and austenite phases were verified by thermodynamic calculations in the temperature range of 873 K to 1273 K (600 °C to 1000 °C). Thermo-Calc,[38] which is a commercial thermodynamic calculating program, was used for the calculation, based on the thermodynamic database of TCFE2000 and its upgraded version.[39,40] Since ferrite, austenite, and κ-carbide are main phases in the Fe-Mn-Al-C—based ($\alpha + \gamma$) duplex lightweight

steels, they are considered in the thermodynamic calculations. According to the thermodynamic database,[39,40] other phases, *e.g.*, cementite, M_5C_2, and M_7C_3, originating from the Fe-Mn-C ternary system and graphite, might appear as stable phases, but these phases are not considered in the calculations because they are not present in the actual microstructures. Figure 1(a) shows fractions of equilibrium phases (ferrite, austenite, and κ-carbide). Here, fractions of phases in the equilibrium phase diagrams are calculated as atomic fractions, which can be converted by mole fractions or mass fractions. In the present study, however, the raw data have been used because variation trends of phase fractions are more important than quantities of phase fractions themselves. The austenite and ferrite equally exist at 1123 K (850 °C), and the fraction of austenite decreases as the temperature decreases. At 943 K (670 °C), κ-carbides begin to precipitate, while the fraction of austenite abruptly decreases. In the present annealing temperature range of 1123 K to 1223 K (850 °C to 950 °C), κ-carbides are not formed. Solute contents existing in the austenite between 873 K and 1273 K (600 °C and 1000 °C) are shown in Figure 1(b). As the austenite fraction decreases, the C and Mn contents increase from the nominal composition by alloying partitioning, while the Al content decreases. The Mn, Al, and C contents are 7.6, 4.6, and 0.6 wt pct, respectively, at 1123 K (850 °C), and are changed to 6.8, 4.7, and 0.47 wt pct, respectively, when the temperature increases to 1223 K (950 °C).

B. *Microstructure*

EBSD phase maps of the A850, A900, and A950 steels, together with grain size and volume fraction of austenite (D_γ and V_γ), are shown in Figures 2(a) through (c). The microstructures exhibit a banded structure elongated along the rolling direction, which is composed of ferrite and austenite bands. This banded structure is frequently observed in ($\alpha + \gamma$) duplex stainless steels and lightweight steels.[41–43] Because of the high content of Al, which acts as a strong ferrite stabilizer, the coarse ferrite solidified from the liquid is not entirely transformed to austenite during homogenization and hot-rolling procedures, which makes it difficult for the austenite to exist as a single phase. This coarse ferrite structure is retained in a banded shape even after hot rolling, because it is not easily broken or recrystallized. The ferrite band consists of coarse ferrite grains, while the austenite band consists of fine ferrite and austenite grains, as indicated by white-dotted lines in Figure 2(a). The volume fraction and grain size of austenite are 0.263 and 1.4 μm, respectively, in the A850 steel. As the annealing temperature increases, austenite grains are coarsened to 2.0 μm in the A900 steel (Figure 2(b)) and then are refined to 1.8 μm in the A950 steel (Figure 2(c)). The shapes of bcc phases in the austenite band of the A950 steel are somewhat different from those of the other steels.

Figures 3(a) through (c) show an image quality (IQ) phase color map and inverse pole figure (IPF) maps of austenite band in the A950 steel. Since the IQ map quantifies the sharpness of diffraction bands, it can serve as a qualitative measure of crystal perfection in terms of its content of lattice defects.[44,45] Perfect crystal regions show a high IQ (light), whereas highly lattice-distorted regions, such as interfacial areas, severely deformed zones, and inclusions, show a lower IQ (dark).[44,45] In the IQ map, the austenite band consists of blue-colored austenite grains and white- or gray-colored bcc phase grains (Figure 3(a)). The gray-colored bcc grains mean that they are highly lattice distorted.[44,45] The IPF map of bcc phase (Figure 3(b)) shows that the gray-colored bcc grains are identified to be α'-martensite having well-developed laths. Thus, the A950 steel consists of
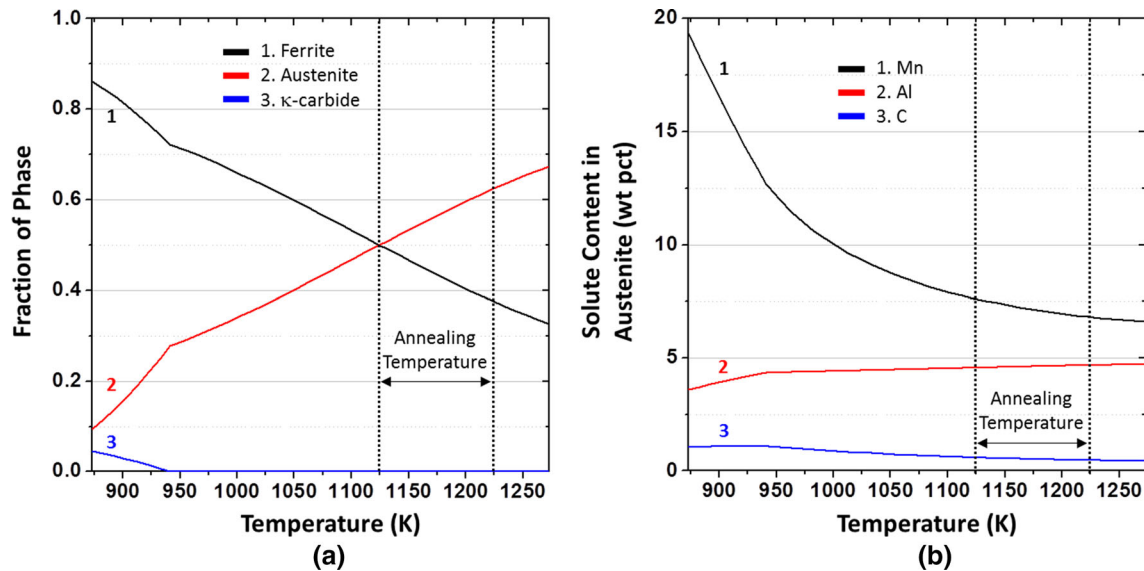

Fig. 1—(*a*) Fractions of the equilibrium phases (ferrite, austenite, and κ-carbide) and (*b*) solute contents in the austenite phase in the temperature range of 873 K to 1273 K (600 °C to 1000 °C).
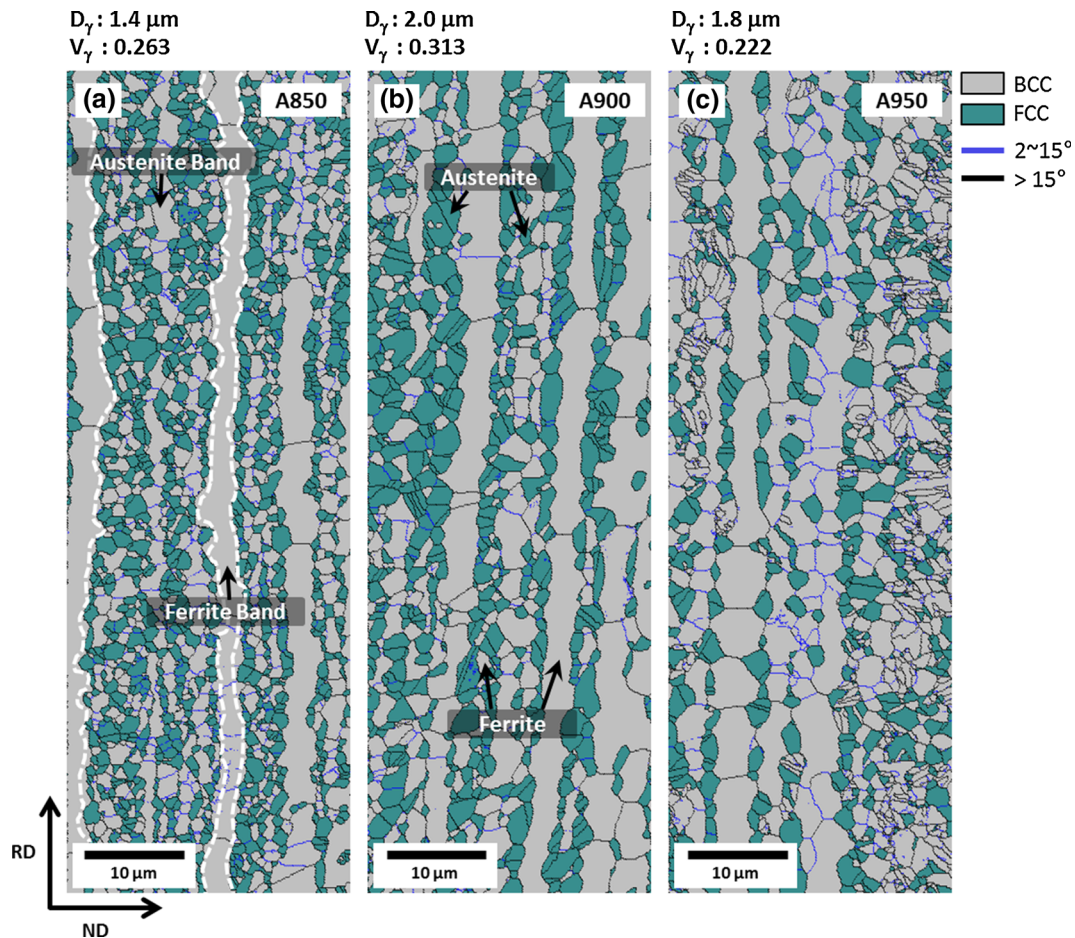
D$_\gamma$: 1.4 μm
V$_\gamma$: 0.263

D$_\gamma$: 2.0 μm
V$_\gamma$: 0.313

D$_\gamma$: 1.8 μm
V$_\gamma$: 0.222

Fig. 2—EBSD phase maps of the (*a*) A850, (*b*) A900, and (*c*) A950 steels. The microstructures basically exhibit a banded structure elongated along the rolling direction, which is composed of ferrite and austenite bands. The ferrite band consists of coarse ferrite grains, while the austenite band consists of fine ferrite and austenite grains.

ferrite, austenite, and α'-martensite. According to the IPF map of austenite (Figure 3(c)), white-dotted lines are identified to be prior austenite grain boundaries because austenite and nearby martensite have the same orientation, which indicates that the martensite located inside a prior austenite grain was transformed from the large prior austenite grain.

The EBSD phase maps of ferrite band of the A850, A900, and A950 steels are shown in Figures 4(a) through (c). In the A850 steel, very few austenite grains are observed in the ferrite band (Figure 4(a)). As the annealing temperature increases, austenite grains are nucleated at ferrite grain boundaries, and their volume fraction increases to 0.154 (Figures 4(b) and (c)). In the A950 steel, already nucleated austenite grains are grown, or new grains are nucleated. Some of them are transformed to α'-martensite during cooling, as indicated by the arrows in Figure 4(c).

C. Tensile Properties

Figure 5 indicates room-temperature tensile engineering stress–strain curves, from which tensile properties are summarized in Table I. The yield and tensile strengths of the A850 steel are 487 and 804 MPa, respectively, while

the elongation is relatively high (56 pct). As the annealing temperature increases from 1123 K to 1223 K (850 °C to 950 °C), the yield strength and elongation decrease, while the tensile strength increases. In the A950 steel, the tensile strength reaches 1056 MPa, but the elongation reduces to 13.5 pct. Figure 6(a) shows true stress–strain curves and strain-hardening rate (dσ/dε) curves, which are indicated by solid and dotted lines, respectively. The three steels show very high true tensile strength of about 1.2 GPa. The strain-hardening rate shows a gradually decreasing behavior after yielding in the A950 steel, whereas it shows a down-up-down behavior in the A850 and A900 steels. In the early stage of strain hardening, the strain-hardening rate increases in the order of A850, A900, and A950 steels.

The volume fractions of austenite were measured by a direct comparison method using XRD analysis, and the results are plotted as a function of true strain in Figure 6(b). Before the tensile deformation, the volume fraction of austenite increases in the order of A950, A850, and A900 steels, which matches the EBSD results in Figures 2(a) through (c). In the A850 steel, the austenite fraction decreases relatively slowly with increasing true strain as a considerable amount of austenite grains transform to α'-martensite, whereas it
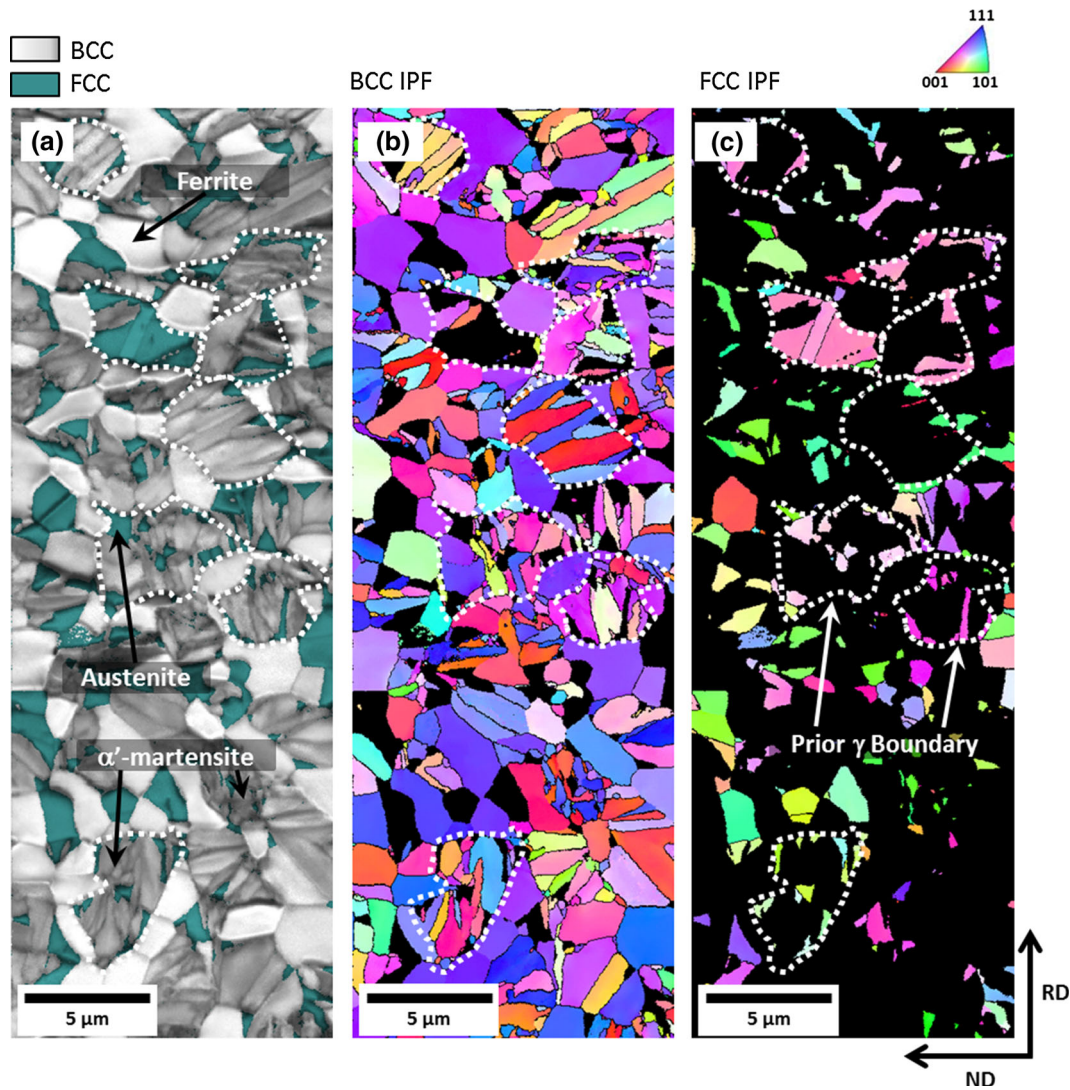
Fig. 3—(a) IQ phase color map, (b) IPF map of bcc phase, and (c) IPF map of fcc phase (austenite) of the A950 steel.

decreases rather rapidly in the A900 and A950 steels. The decreased amount of austenite fraction is largest in A900 steel. EBSD phase maps of the cross-sectional area beneath the fracture surface are shown in Figures 7(a) through (c). Most of the austenite grains are transformed to α′-martensite by a TRIP mechanism, and the resultant volume fraction of austenite decreases below 0.06 in the three steels. Deformation twins or ε-martensite are not found at all, which corresponds to previous research.[4–6]

D. Tensile Deformation Behavior

In order to investigate the tensile deformation behavior in detail, the cross-sectional areas beneath the fracture surface of the tensile specimen were analyzed by SEM, as shown in Figures 8 through 10. These SEM micrographs are classified by initial, intermediate, and final stages according to the extent of deformation or the distance from fracture surface. In the initial stage of the A850 steel, where ferrite and austenite bands are distinguished clearly, deformation bands are weakly initiated inside ferrite bands (Figure 8(a)), while a few

martensite phases are formed inside austenite bands, as marked by arrows in Figure 8(b). As the deformation proceeds into the intermediated stage, deformation bands are actively developed in austenite bands as well as ferrite bands (Figure 8(c)), and most of the austenite grains are transformed to martensite (Figure 8(d)). Common failure sites of martensite are martensite/ferrite interfaces or martensite phases themselves, which lead to the formation of microvoids or microcracks, respectively.[46] With further deformation, deformation bands are deepened inside ferrite bands and microvoids are initiated at martensite/ferrite interfaces inside austenite bands (Figures 8(e) and (f)).

In the A900 steel, the overall deformation behavior is similar to that of the A850 steel. In the initial deformation stage, a considerable number of martensite phases are formed inside austenite bands by the γ/α′ transformation, while deformation bands are weakly formed inside ferrite bands (Figures 9(a) and (b)). In the next deformation stage, most austenite grains inside austenite bands are transformed to martensite, and microvoids or microcracks are formed at martensite/ferrite interfaces
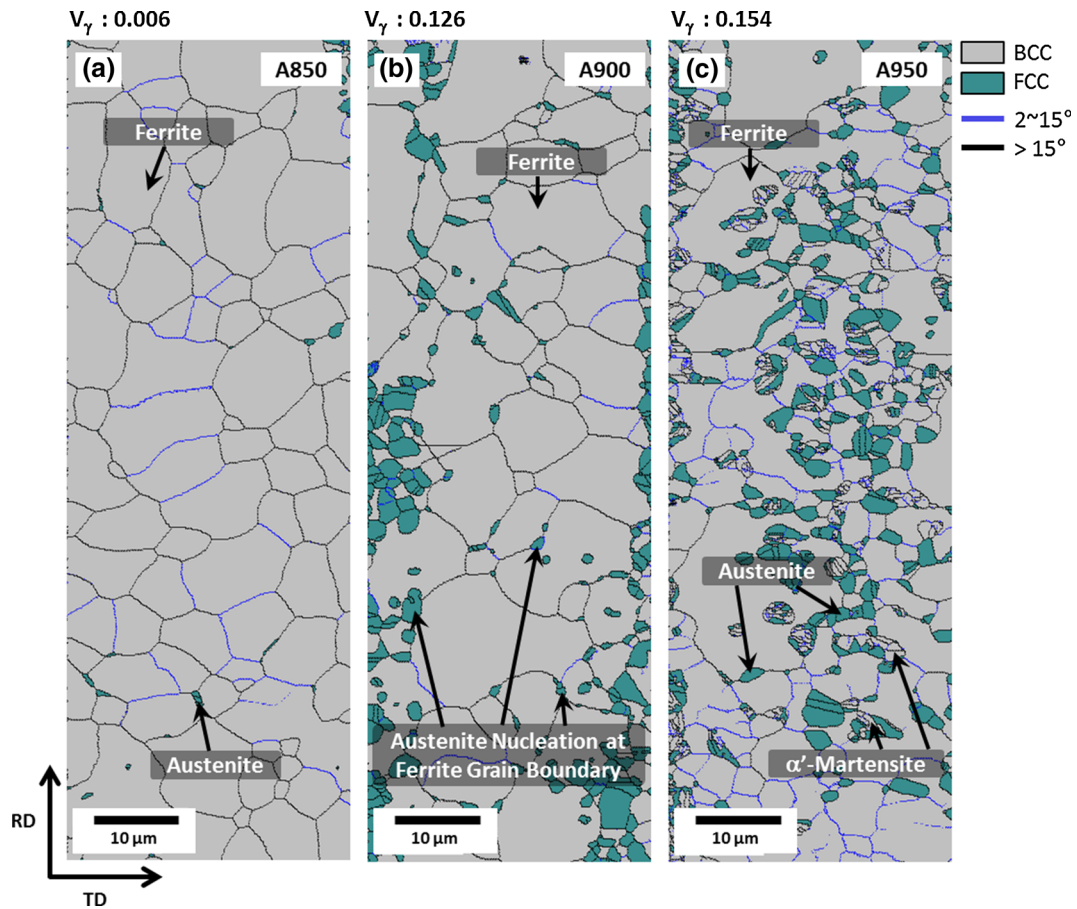
Fig. 4—EBSD phase maps of ferrite band of the (*a*) A850, (*b*) A900, and (*c*) A950 steels. Austenite grains are nucleated at ferrite grain boundaries in the A900 and A950 steels, and their volume fractions range from 0.126 to 0.154.
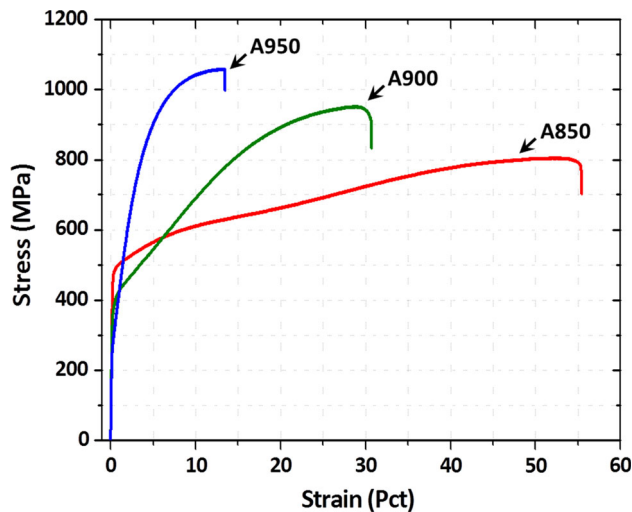

Fig. 5—Room-temperature tensile engineering stress–strain curves of the A850, A900, and A950 steels. As the annealing temperature increases, the yield strength and elongation decrease, while the tensile strength increases.

or martensite phases themselves (Figures 9(c) and (d)). It is not likely that deformation bands are actively formed inside ferrite bands.

In the A950 steel containing a considerable number of martensite phases prior to tensile deformation, microvoids or microcracks are initiated at martensite/ferrite interfaces or martensite phases right after tensile deformation, while deformation bands are hardly developed inside ferrite bands (Figures 10(a) and (b)). As the deformation proceeds further, microvoids or microcracks are propagated into ferrite bands or austenite bands to form long cleavage cracks (Figures 10(c) and (d)).

The SEM fractographs of the fractured tensile specimen are shown in Figures 11(a) through (c). In the A850 steel, a ductile-dimpled fracture is predominant because deformation bands are well developed in wide areas (Figure 11(a)). In the A900 and A950 steels, the fracture occurs in a mixed mode of quasi-cleavage fracture and cleavage fracture (Figures 11(b) and (c)). The cleavage fracture mode prevails more in the A950 steel.

IV. DISCUSSION

The volume fraction of austenite increases with increasing annealing temperature, as shown in the thermodynamic calculation data (Figure 1(a)). In the A950 steel, however, it decreases as many austenite

Table I. Room-Temperature Tensile Test Results of the Three Annealed Lightweight Steels

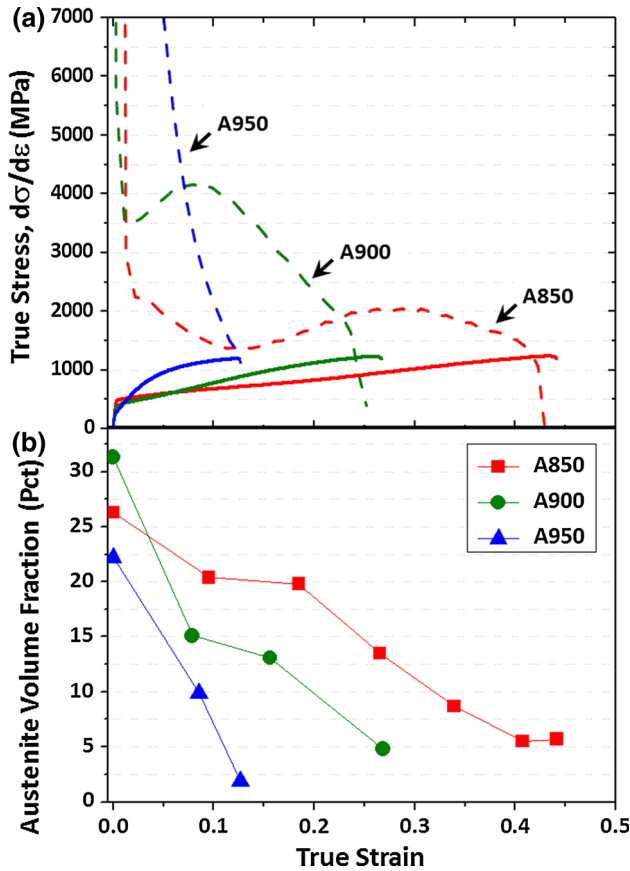| Steel	Yield Strength (MPa)	Tensile Strength (MPa)	Elongation (Pct)
A850	487 ± 10	804 ± 13	55.5 ± 1.2
A900	385 ± 1	950 ± 12	30.8 ± 1.5
A950	308 ± 4	1056 ± 8	13.5 ± 0.8

Fig. 6—(a) True stress–strain and strain-hardening rate curves and (b) austenite volume fraction of the A850, A900, and A950 steels. The volume fractions of austenite were measured by a direct comparison method using XRD analysis.

grains are transformed to martensite, as shown in Figures 2 through 4. This is because the thermal stability of austenite is deteriorated by the decrease in C and Mn contents (Figure 1(b)), the increase in volume fraction of austenite, and the coarsening of austenite grains (Figure 2(c)). This increase in austenite grain size readily provides nucleation sites for stacking faults and shear-band intersections.[47] It also promotes the transformation to martensite due to the decrease in strain energy required for lattice distortion and shear deformation.[45,46] The effects of alloying elements and grain sizes on martensite start temperature (M_s) can be explained by the following equations suggested by Jimenez-Melero et al.[48] and Mahieu et al.[36]:

$$M_{s0}(K) = 539 - 423C - 30.4Mn - 7.5Si + 30Al + 273 \quad [2]$$

$$M_s(K) = M_{s0} - B\left(V_\gamma^{-1/3}\right) \quad [3]$$

where M_{s0} shows the effect of alloying composition; V_γ and B are the average volume and geometry coefficient (475 μm K) of austenite grain, respectively. The C, Mn, and Al contents, austenite grain size, and the M_s of the three annealed steels are shown in Table II. Here, C, Mn, and Al contents are measured from the XRD and EPMA analyses. In the M_s calculation of the A950 steel, the prior austenite grain size measured from white-dotted areas in Figures 3(a) through (c) (2.6 μm) is used, because the austenite grain size measured from the EBSD phase map (Figure 2(c)) is underestimated by the martensite formed during cooling.

When the annealing temperature increases from 1123 K to 1223 K (850 °C to 950 °C), the contents of C and Mn in the austenite are reduced by 0.13 and 0.81 wt pct, respectively, while the content of Al increases slightly. The grain sizes of austenite are 1.4 and 2.6 μm in the A850 and A950 steels, respectively, which indicates about an increase of two times in grain size. The effect of alloying composition (M_{s0}) is calculated to be 738 K to 820 K (465 °C to 547 °C) in the three steels, because the contents of C and Mn decrease with increasing austenite volume fraction, which shows the higher M_{s0} by 82 K (82 °C) in the A950 steel. When the austenite grain size is considered, the M_s of the A950 steel is calculated to be 320 K (47 °C), which is higher by 288 K (288 °C) than that of the A850 steel. This implies that the martensite can be formed during cooling without any deformation in the A950 steel. As a result of the existence of athermal α'-martensite, thus, the volume fraction and size of austenite of the A950 steel are lower or smaller than those of the A900 steel (Figures 2(b) and (c)).

This variation in austenite stability greatly affects the tensile properties of the annealed steels as well as the microstructural evolution. The decrease in yield strength with increasing annealing temperature can be explained by the coarsening of grains due to the Hall–Petch relation and the presence of α'-martensite in the A950 steel. Dislocations are nucleated at nearby ferrite boundaries by the shear strain and volume change induced by γ/α' transformation, but dislocations nucleated near the martensite are not pinned.[49,50] These martensite-induced dislocations are moved even at low stress levels, which reduces the yield strength and causes the high strain-hardening rate with further deformation.[50]

According to Figure 6(a), the strain-hardening rate shows a down-up-down behavior in the A850 and A900 steels, and starts to increase at the true strain of 0.15 and
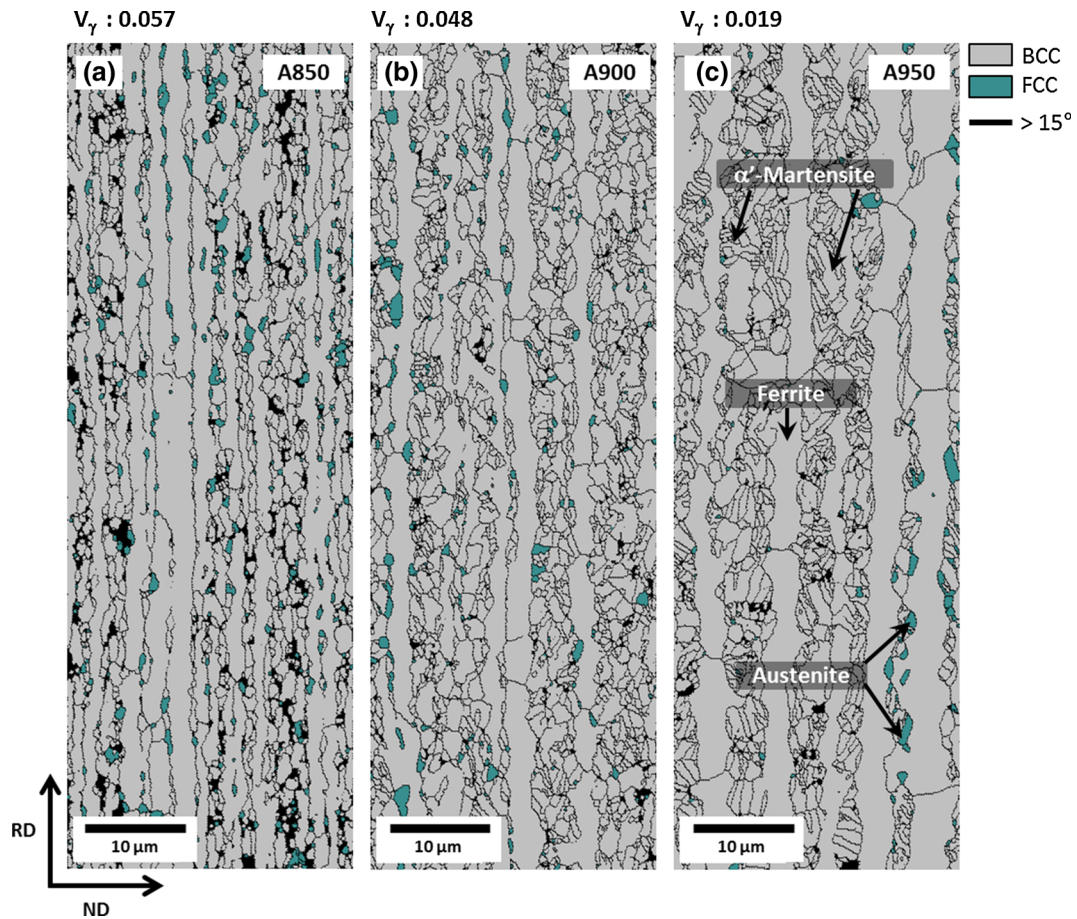
Fig. 7—EBSD phase maps of the cross-sectional area beneath the fracture surface of the (*a*) A850, (*b*) A900, and (*c*) A950 steels. Most austenite grains are transformed to martensite by a TRIP mechanism, and the resultant volume fraction of austenite decreases below 0.06 in the three steels.

0.02, respectively. As learned from the variation in austenite volume fraction (Figure 6(b)), the increasing range of strain-hardening rate is attributed to the activation of strain-induced γ/α' transformation. In the A850 steel, the stability of austenite is highest because of the grain refinement and high contents of C and Mn; thus, the deformation of true strain of 0.15 is required to trigger the active TRIP mechanism. Since the strain-induced γ/α' transformation needs a considerable amount of deformation, a sufficient number of deformation bands are formed at ferrite grains in the initial stage of deformation in both austenite and ferrite bands (Figures 8(a) and (b)). When the deformation proceeds further, microvoids are initiated at austenite/martensite interfaces inside austenite bands, but their coalescence and propagation procedures are very slow to reach final failure (Figures 8(e) and (f)). Since ferrite grains take over most of the strains as deformation bands are sufficiently formed, the fracture occurs in a ductile-dimpled fracture mode (Figure 11(a)). When the γ/α' transformation rate is appropriate, as in the A850 steel, most of the strains are relatively homogeneously distributed into austenite grains as well as ferrite grains, which results in a good combination of strength and ductility (Table I).

In the A900 steel whose austenite stability is lower than that of the A850 steel, the strain required for the active γ/α' transformation is lower, and the strain-hardening rate is higher because of the higher γ/α' transformation rate. In the initial stage of deformation, deformation bands are not well developed inside ferrite and austenite bands (Figures 9(a) and (b)). The higher γ/α' transformation rate than the A850 steel results in higher tensile strength, but provides more microvoids or microcrack initiation sites at martensite/ferrite interfaces or martensite phases (Figures 9(c) and (d)). In the case of decreased austenite stability, as in the A900 steel, thus, the deformation strain works for the γ/α' transformation rather than the formation of deformation bands, thereby leading to higher strength and lower elongation.

The A950 steel already contains a considerable number of martensite phases before the tensile deformation. Its strain-hardening rate is highest in the initial stage of deformation (Figure 6(a)), and the austenite volume fraction rapidly decreases (Figure 6(b)). Since the austenite stability and required deformation amount are lowest, deformation bands are not formed at ferrite grains in both austenite and ferrite bands (Figures 10(a) and (b)). Microvoids or microcracks readily initiate at
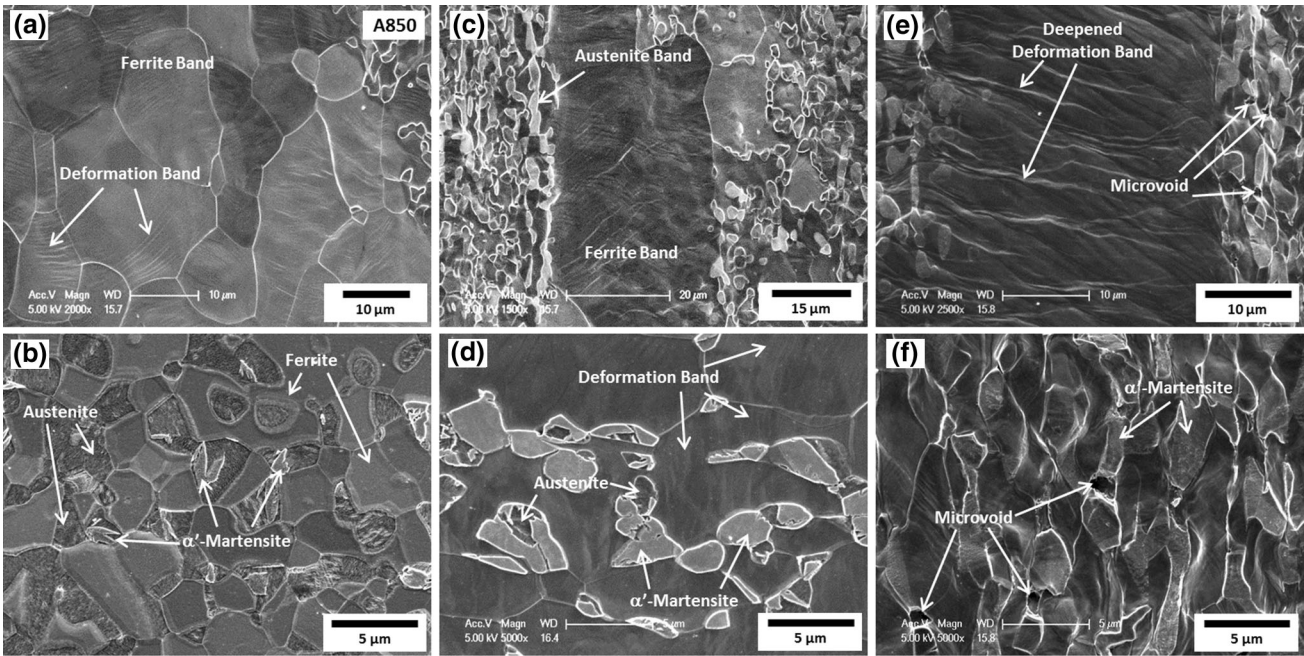
Fig. 8—SEM micrographs of the cross-sectional area beneath the fracture surface of the tensile specimen of the A850 steel, showing (*a*) and (*b*) deformation bands weakly initiated inside ferrite bands and a few martensite phases inside austenite bands, (*c*) and (*d*) deformation bands developed in austenite and ferrite bands and many martensite phases transformed from austenite grains, and (*e*) and (*f*) deepened deformation bands inside ferrite bands and microvoids initiated at martensite/ferrite interfaces inside austenite bands. These SEM micrographs are classified by initial, intermediate, and final stages according to the extent of the deformation.
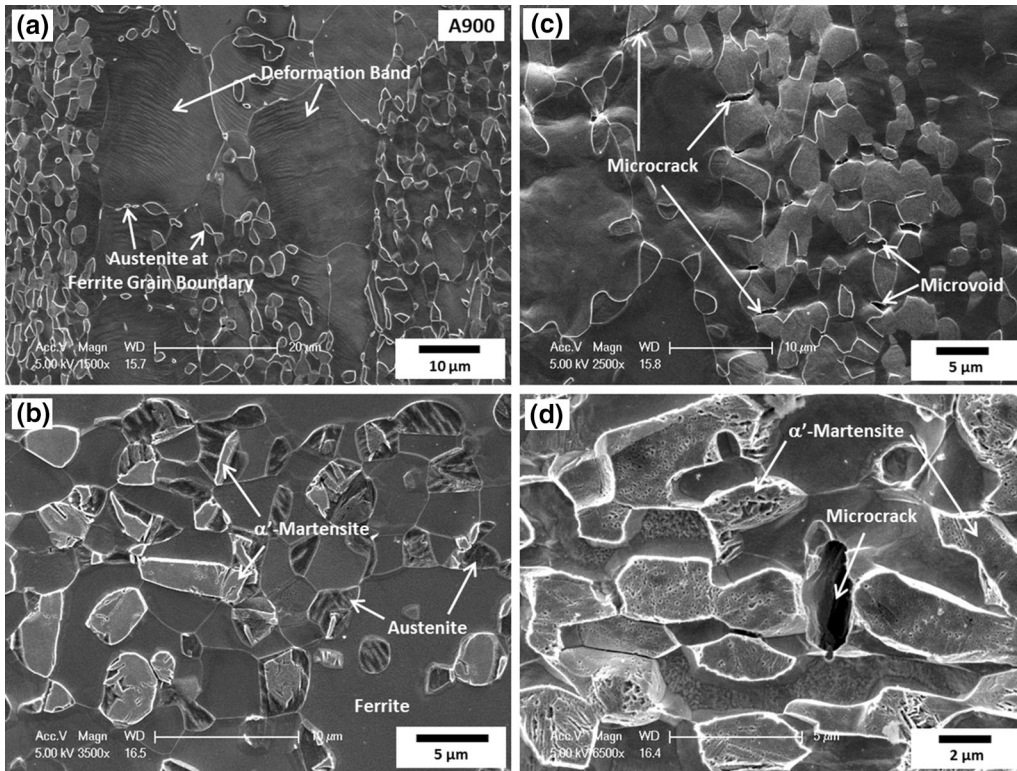

Fig. 9—SEM micrographs of the cross-sectional area beneath the fracture surface of the tensile specimen of the A900 steel, showing (*a*) and (*b*) deformation bands weakly formed inside ferrite bands and martensite phases formed by γ/α' transformation inside austenite bands and (*c*) and (*d*) microvoids or microcracks formed at martensite/ferrite interfaces or martensite phases.
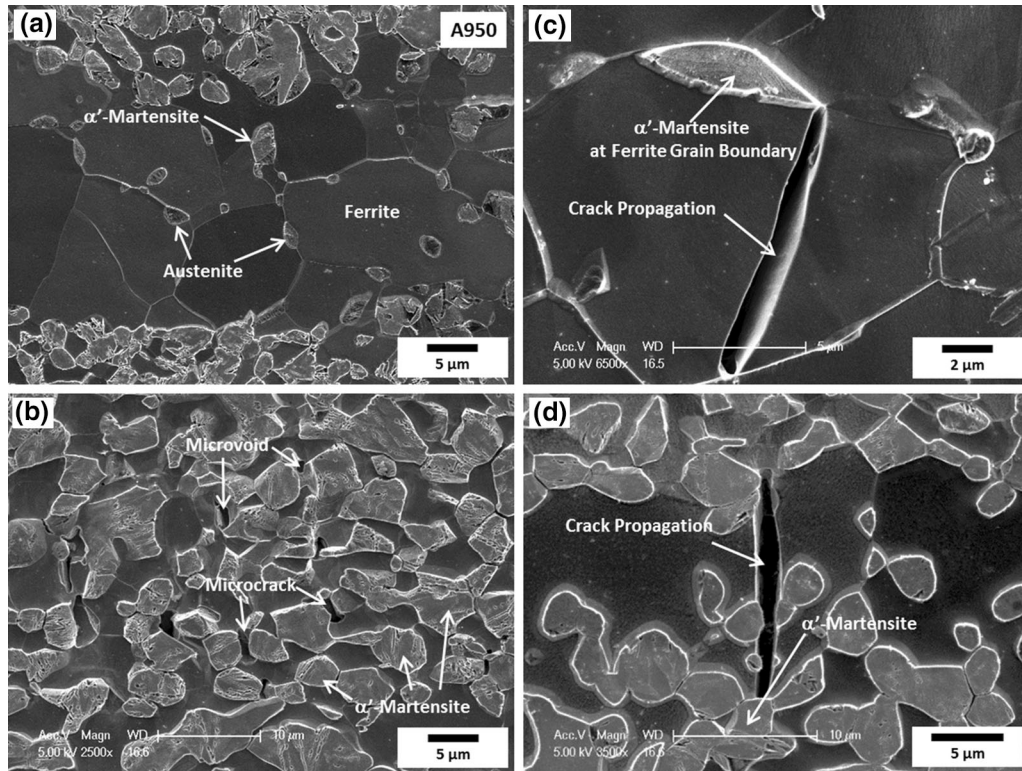
Fig. 10—SEM micrographs of the cross-sectional area beneath the fracture surface of the tensile specimen of the A950 steel, showing (*a*) and (*b*) microvoids or microcracks initiated at martensite/ferrite interfaces or martensite phases inside austenite bands and (*c*) and (*d*) propagation of microvoids or microcracks into ferrite or austenite bands to form long cleavage cracks.
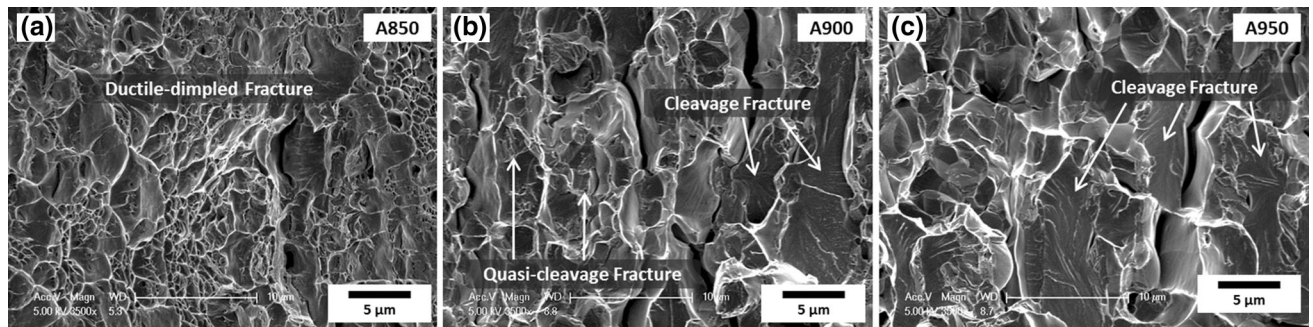

Fig. 11—SEM fractographs of the tensile specimens of the (*a*) A850, (*b*) A900, and (*c*) A950 steels. A ductile-dimpled fracture mode is predominant in the A850 steel, whereas a mixed mode of quasi-cleavage fracture and cleavage fracture is observed in the A900 and A950 steels.

Table II.   C, Mn, and Al Contents, Austenite Grain Size, and Martensite Start Temperature (M_s) of the Three Annealed Lightweight Steels

Steel	C* (Wt Pct)	Mn** (Wt Pct)	Al** (Wt Pct)	Austenite Grain Size (μm)	$M_{s0}^{\dagger}$ [K (°C)]	$M_s^{\ddagger}$ [K (°C)]
A850	0.60	7.63	4.57	1.4 ± 0.5	738 (465)	32 (−241)
A900	0.53	7.15	4.63	2.0 ± 0.7	784 (511)	215 (−58)
A950	0.47	6.82	4.68	2.6 ± 0.7†	820 (547)	320 (47)

*Content of C measured from the XRD analysis.
**Contents of Mn and Al measured from the EPMA analysis.
† Prior austenite grain size measured from white-dotted areas in Figs. 3(a) through (c).
‡ M_s temperatures calculated from Eqs. [1] and [2].

martensite/ferrite interfaces or martensite phases even at a low strain level and propagate across ferrite grains to form cleavage cracks (Figures 10(c) and (d)). This results in a major fracture mode of cleavage on the fracture surface (Figure 11(c)). In the A950 steel, the deformation is concentrated in austenite grains and

martensite without forming deformation bands at ferrite grains because of the most active γ/α' transformation, which results in the highest strength and lowest elongation (Figure 5 and Table I).

In the present intercritically annealed medium-Mn lightweight steels containing austenite and martensite in the ferrite matrix, the formation of martensite is desirable for the tensile strength. When considering the strength and elongation simultaneously, austenite grains having an appropriate stability for the formation of strain-induced martensite are desirable. Since austenite grains and their stability greatly affect tensile properties, they do not sufficiently contribute to the ductility improvement in the A950 steel having very low stability. In order to obtain the best combination of strength and ductility, thus, the formation of austenite having an appropriate stability, i.e., highest stability in the present case, is needed, and can be achieved when 0.26 of fine austenite (size: 1.4 μm) is homogenously distributed in the ferrite matrix, as in the A850 steel. This best combination of strength and ductility is attributed to the requirement of sufficient deformation for strain-induced γ/α' transformation and the formation of many deformation bands at ferrite grains in austenite and ferrite bands, as most of strains are homogeneously distributed into austenite grains as well as ferrite grains. Since this steel has excellent strength and ductility as well as reduced costs of alloying elements and weight savings, it holds promise for automotive applications requiring excellent mechanical properties.

V. CONCLUSIONS

Medium-Mn duplex lightweight steels were developed by varying the intercritical-annealing temperature of an Fe-0.32C-5.8Mn-5Al (wt pct) steel, and their tensile properties were explained by the stability of austenite, which played an important role in the TRIP mechanism.

1. In the 1123 K (850 °C)—annealed steel, the stability of austenite was highest because of the grain refinement and high contents of C and Mn; thus, the largest deformation was required for triggering the active TRIP mechanism among the three annealed steels. Since the TRIP needed a considerable amount of deformation, many deformation bands were formed at ferrite grains in both austenite and ferrite bands. As ferrite grains took over most of the strains by sufficiently forming deformation bands, an excellent combination of strength and ductility was achieved.
2. Since the 1223 K (950 °C)—annealed steel already contained a considerable amount of martensite before tensile deformation, the strain-hardening rate was very high and the austenite stability and deformation amount required for the TRIP were lowest among the three annealed steels. Deformation bands were not formed at ferrite grains and microvoids or microcracks readily initiated at martensite/ferrite interfaces or martensite phases even at a low strain level, thereby leading to very

low ductility in spite of the high tensile strength.
3. In order to obtain the best combination of strength and ductility by the TRIP mechanism, the formation of austenite having an appropriate stability, i.e., highest stability in the present case, was needed and could be achieved when fine austenite grains (size: 1.4 μm, volume fraction: 0.26) were homogenously distributed in the ferrite matrix, as in the 1123 K (850 °C)—annealed steel. Since this medium-Mn lightweight steel has excellent tensile properties as well as reduced alloying costs and weight savings, it shows promise for new automotive applications.

REFERENCES

1. A. Mayyas, A. Qattawi, M. Omar, and D. Shan: *Renew. Sustain. Energy Rev.*, 2012, vol. 16, pp. 1845–62.
2. R. Kuziak, R. Kawalla, and S. Waengler: *Arch. Civ. Mech. Eng.*, 2008, vol. 8, pp. 103–17.
3. S.W. Hwang, J.H. Ji, E.G. Lee, and K.-T. Park: *Mater. Sci. Eng. A*, 2011, vol. 528, pp. 5196–5203.
4. C.-H. Seo, K.H. Kwon, K. Choi, K.-H. Kim, J.H. Kwak, S. Lee, and N.J. Kim: *Scripta Mater.*, 2012, vol. 66, pp. 519–22.
5. S.-J. Park, B. Hwang, K.H. Lee, T.-H. Lee, D.-W. Suh, and H.N. Han: *Scripta Mater.*, 2013, vol. 68, pp. 365–69.
6. D.-W. Suh, S.-J. Park, T.-H. Lee, C.-S. Oh, and S.-J. Kim: *Metall. Mater. Trans. A*, 2010, vol. 41A, pp. 397–408.
7. L. Remy and A. Pineau: *Mater. Sci. Eng.*, 1977, vol. 28, pp. 99–107.
8. H.W. Zhang, Z.K. Hei, G. Liu, J. Lu, and K. Lu: *Acta Mater.*, 2013, vol. 51, pp. 1871–81.
9. A. Dumay, J.-P. Chateau, S. Allain, S. Migot, and O. Bouaziz: *Mater. Sci. Eng.*, 2008, vol. A483–A484, pp. 184–87.
10. O. Bouaziz, S. Allain, C.P. Scott, P. Cugy, and D. Barbier: *Curr. Opin. Solid State Mater. Sci.*, 2011, vol. 15, pp. 141–68.
11. T. Sahraoui, M. Hadji, and M. Yahi: *Mater. Sci. Eng. A*, 2009, vol. 523, pp. 271–76.
12. J.E. Jung, J. Park, J.-S. Kim, J.B. Jeon, S.K. Kim, and Y.W. Chang: *Metall. Mater. Int.*, 2014, vol. 20, pp. 27–34.
13. G. Frommeyer and U. Brüx: *Steel Res. Int.*, 2006, vol. 77, pp. 627–33.
14. R. Rana, C. Liu, and R.K. Ray: *Scripta Mater*, 2013, vol. 68, pp. 354–59.
15. S.S. Sohn, H. Song, B.-C. Suh, J.-H. Kwak, B.-J. Lee, N.J. Kim, and S. Lee: *Acta Mater.*, 2015, vol. 96, pp. 301–10.
16. H. Huang, D. Gan, and P.W. Kao: *Scripta Metall. Mater.*, 1994, vol. 30, pp. 499–504.
17. W.K. Choo, J.H. Kim, and J.C. Yoon: *Acta Mater.*, 1997, vol. 45, pp. 4877–85.
18. K. Sato, K. Tagawa, and Y. Inoue: *Metall. Trans. A*, 1990, vol. 21A, pp. 5–11.
19. C.L. Lin, C.G. Chao, H.Y. Bor, and T.F. Liu: *Mater. Trans.*, 2010, vol. 51, pp. 1084–88.
20. K.T. Luo, P.-W. Kao, and D. Gan: *Mater. Sci. Eng. A*, 1992, vol. 151, pp. L15–L18.
21. S.Y. Han, S.Y. Shin, H.-J. Lee, B.-J. Lee, S. Lee, N.J. Kim, and J.-H. Kwak: *Metall. Mater. Trans. A*, 2012, vol. 43A, pp. 843–53.
22. G. Frommeyer, E.J. Drewes, and B. Engl: *Rev. Metall. Cah. Inf. Technol.*, 2000, vol. 97, pp. 1245–53.

23. L. Falat, A. Schneider, G. Sauthoff, and G. Frommeyer: *Intermetallics*, 2005, vol. 13, pp. 1256–62.
24. Y. Sutou, N. Kamiya, R. Umino, I. Ohnuma, and K. Ishida: *ISIJ Int.*, 2010, vol. 50, pp. 893–99.
25. K. Choi, C.-H. Seo, H. Lee, S.K. Kim, J.H. Kwak, K.G. Chin, K.-T. Park, and N.J. Kim: *Scripta Mater.*, 2010, vol. 63, pp. 1028–31.
26. K.-T. Park, K.G. Jin, S.H. Han, S.W. Hwang, K. Choi, and C.S. Lee: *Mater. Sci. Eng. A*, 2010, vol. 527, pp. 3651–61.
27. B. Kim, T.T.T. Trang, and N.J. Kim: *Met. Mater. Int.*, 2014, vol. 20, pp. 35–39.
28. H. Kim, D.-W. Suh, and N.J. Kim: *Sci. Technol. Adv. Mater.*, 2013, vol. 14, pp. 1–11.
29. S.S. Sohn, B.-J. Lee, S. Lee, and J.-H. Kwak: *Met. Mater. Int.*, 2015, vol. 21, pp. 43–53.
30. K.-G. Chin, C.-Y. Kang, S.Y. Shin, S. Hong, S. Lee, H.S. Kim, K.-H. Kim, and N.J. Kim: *Mater. Sci. Eng. A*, 2011, vol. 528, pp. 2922–28.
31. O. Grässel, L. Krüger, G. Frommeyer, and L.W. Meyer: *Int. J. Plast.*, 2000, vol. 16, pp. 1391–1409.
32. J.H. Ryu, D.-I. Kim, H.S. Kim, H.K.D.H. Bhadeshia, and D.-W. Suh: *Scripta Mater.*, 2010, vol. 63, pp. 297–99.
33. A. Zargaran, H.S. Kim, J.H. Kwak, and N.J. Kim: *Met. Mater. Int.*, 2015, vol. 21, pp. 79–84.
34. S.S. Sohn, B.-J. Lee, J.-H. Kwak, and S. Lee: *Metall. Mater. Trans. A*, 2014, vol. 45A, pp. 3844–56.
35. S.S. Babu, E.D. Specht, S.A. David, E. Karapetrova, P. Zschack, M. Peet, and H.K.D.K. Bhadeshia: *Metall. Mater. Trans. A*, 2005, vol. 36A, pp. 3281–89.
36. J. Mahieu, J. Maki, B.C. De Cooman, and S. Claessens: *Metall. Mater. Trans. A*, 2002, vol. 33A, pp. 2573–80.
37. B.D. Cullity: in *Elements of X-Ray Diffraction*, 2nd ed., M. Cohen, ed., Addison-Wesley, Reading, MA, 1978, pp. 517–18.
38. B. Sundman, B. Jansson, and J.-O. Andersson: *Calphad*, 1985, vol. 9, pp. 153–90.
39. "TCFE2000: *The Thermo-Calc Steels Database*, upgraded by B.-J. Lee, B. Sundman at KTH," KTH, Stockholm, 1999.
40. K.-G. Chin, H.-J. Lee, J.-H. Kwak, J.-Y. Kang, and B.-J. Lee: *J. Alloys Compd.*, 2010, vol. 505, pp. 217–23.
41. A. Piñol-Juez, A. Iza-mendia, and I. Gutiérrez: *Metall. Mater. Trans. A*, 2000, vol. 31A, pp. 1671–77.
42. N. Suutala, T. Takalo, and T. Moisio: *Metall. Trans. A*, 1980, vol. 11A, pp. 717–25.
43. S. Atamert and J.E. King: *Acta Metall. Mater.*, 1991, vol. 39, pp. 273–85.
44. C. Herrera, D. Ponge, and D. Raabe: *Acta Mater.*, 2011, vol. 59, pp. 4653–64.
45. F.J. Humphreys, P.S. Bate, and P.J. Hurley: *J. Microsc.*, 2001, vol. 201, pp. 50–58.
46. D. Yan, C.C. Tasan, and D. Raabe: *Acta Mater.*, 2015, vol. 96, pp. 399–409.
47. S. Takaki, K. Fukunaga, J. Syarif, and T. Tsuchiyama: *Mater. Trans.*, 2004, vol. 45, pp. 2245–51.
48. E. Jimenez-Melero, N.H. van Dijk, L. Zhao, J. Sietsma, S.E. Offerman, J.P. Wright, and S. van der Zwaag: *Scripta Mater.*, 2007, vol. 56, pp. 421–24.
49. M. Mazinani and W.J. Poole: *Metall. Mater. Trans. A*, 2007, vol. 38A, pp. 328–39.
50. G. Krauss: *Steels: Processing, Structure, and Performance*, 2nd ed., ASM International, Ohio, 2015, p. 234.